

# Contents lists available at ScienceDirect

# Placenta

journal homepage: www.elsevier.com/locate/placenta





# Low field combined diffusion-relaxation MRI for mapping placenta structure and function

Paddy J. Slator <sup>a,b,c,\*</sup>, Jordina Aviles Verdera <sup>e,f</sup>, Raphael Tomi-Tricot <sup>d,e,f</sup>, Joseph V. Hajnal <sup>e,f</sup>, Daniel C. Alexander <sup>a</sup>, Jana Hutter <sup>e,f</sup>

- a Centre for Medical Image Computing and Department of Computer Science, University College London, London, United Kingdom
- <sup>b</sup> Cardiff University Brain Research Imaging Centre, School of Psychology, Cardiff University, Cardiff, United Kingdom
- School of Computer Science and Informatics, Cardiff University, Cardiff, United Kingdom
- <sup>d</sup> MR Research Collaborations, Siemens Healthineers Limited, Camberley, United Kingdom
- e Centre for the Developing Brain, School of Biomedical Engineering and Imaging Sciences, King's College London, London, United Kingdom
- f Biomedical Engineering Department, School of Biomedical Engineering and Imaging Sciences, King's College London, London, United Kingdom

#### ARTICLE INFO

#### Keywords: MRI Diffusion MRI Combined diffusion-relaxation T2\*

#### ABSTRACT

*Introduction:* Combined diffusion-relaxation MRI shows potential for improved characterisation of pregnancy complications. All existing diffusion-relaxation studies in the placenta are at high field strength, mostly 3T. Here we demonstrate quantitative multi-parametric mapping in the placenta with combined T2\*-diffusion MRI at low-field strength (0.55T).

Methods: We present 56 placental MRI scans performed on a commercially available 0.55T scanner. We acquired the images using a combined T2\*-diffusion technique that simultaneously acquires multiple diffusion preparations and echo times. We processed the data to produce quantitative T2\* and diffusivity maps using a combined T2\*-ADC model. We compared the derived quantitative parameters across gestation in healthy controls and a cohort of clinical cases.

Results: Quantitative parameter maps show similar spatial patterns, but different absolute values, to previous experiments at high field strength, with similar trends in T2\* and ADC against gestational age observed. Discussion: Combined T2\*-diffusion placental MRI is reliably achievable at 0.55T. The advantages of low-field imaging - such as reduced cost, ease of deployment, improved accessibility, greater patient comfort due to the wider bore, and longer T2\* values enabling greater absolute range - can support the broader adoption of quantitative placental MRI techniques, such as combined T2\*-diffusion, as a complementary tool to ultrasound during pregnancy.

# 1. Introduction

The placenta is vital to the health of mother and baby during pregnancy, performing the role of all organs and enabling exchange of oxygen, nutrients, and removal of waste products [1,2]. Placental dysfunction is a primary cause of many common pregnancy complications, such as stillbirth, fetal growth restriction (FGR), and pre-eclampsia [3]. However, human placental development remains poorly understood due to the difficulty of direct in-vivo observation [4]. Non-invasive biomarkers of human placental structure and function during pregnancy are therefore of great interest and can ultimately contribute to new techniques suitable for the prediction, diagnosis, and

monitoring of pregnancy complications. This is particularly timely as there are potential treatments emerging for complications such as pre-eclampsia and FGR [5], which will be most effective if diagnosis is early and specific.

Placental MRI is a promising technique for diagnosis, prognosis and monitoring of multiple pregnancy complications including fetal growth restriction (FGR) [6] and pre-eclampsia (PE) [7]. In particular, T2\* relaxometry is emerging as a tool for detecting pregnancy complications [8–11], with T2\* reduced in FGR and PE [12,13]. The apparent diffusion coefficient (ADC) derived from diffusion MRI (dMRI) also shows promise as a biomarker, with lower ADC values in FGR [14–16]. The more complex dMRI intravoxel incoherent motion (IVIM) model is also

<sup>\*</sup> Corresponding author. Centre for Medical Image Computing and Department of Computer Science, University College London, London, United Kingdom *E-mail address:* slatorp@cardiff.ac.uk (P.J. Slator).

sensitive to pregnancy complications [17–21]. Recent *combined dif-fusion-relaxation* approaches merge relaxometry and dMRI into a single scan that accounts for correlations between relaxation and diffusion properties and can hence disentangle complex microenvironments that cannot be distinguished with diffusion or relaxation MRI alone [22]. Combined diffusion-relaxation has been demonstrated for T2-diffusion [23] and T2\*-diffusion [24,25] in the placenta, and shows initial promise for detecting a range of pregnancy complications at 3T [13,24, 26]. However, the added value of these combined measurements over individual diffusion and relaxation measurements has yet to be definitively established.

Although placental MRI shows promise as a screening tool, there are several drawbacks that hinder widespread adoption. These include the high cost and time requirements associated with MRI scanning compared to ultrasound. This is especially pertinent for quantitative techniques such as T2\* and dMRI, which require the acquisition of multiple volumes. Motion due to maternal breathing and fetal movement is another significant problem, as are uterine contractions which can necessitate discarding affected data. Additionally, combined diffusion-relaxation MRI necessitates longer protocols than single T2\* and dMRI scans, exacerbating the issue. Furthermore, these techniques are typically based on single-shot Echo Planar Imaging (EPI) which, due to its low bandwidth, is sensitive to field inhomogeneities, such as at airtissue boundaries.

Low-field MRI offers multiple advantages over high-field [27], and hence has the potential to enable widespread use of placental MRI. In particular, low-field MRI is generally cheaper to operate and easier to deploy. A 0.55T MRI system is estimated to be 40-50 % cheaper than 1.5T [28]. Consequently, low-field MRI can help widen access to antenatal MRI beyond specialist centres. Some, although not all, low-field MRI scanners also have a wider bore, potentially expanding accessibility to the growing pregnant population with obesity whilst maintaining field homogeneity, hence offering less susceptibility-induced distortions. The possibility of increased space within a wide bore, alongside lower acoustic noise, can also increase patient comfort. Furthermore, the longer T2\* relaxation time, provides a greater absolute range, which could enable clearer discrimination between controls and cases, particularly given the low T2\* values that are typically observed in late gestation and pathological cases. However, low-field MRI does come with trade-offs, the most significant being lower SNR, which necessitates longer scan times and/or larger voxel sizes.

In this paper, we demonstrate the feasibility of combined T2\*-diffusion MRI at low-field, showing that the potential benefits of both techniques can be jointly realised. We first describe how we adapt a previously demonstrated multi-echo gradient-echo diffusion-weighted single-shot EPI sequence to a commercially available low-field scanner. We then calculate quantitative parameter maps from the low-field data and show reasonable compatibility with those derived at higher field strengths. Our first demonstration motivates broader studies of low-field combined diffusion-relaxation placental MRI for widespread pregnancy monitoring.

# 2. Methods

Pregnant women were recruited at St Thomas' Hospital, a tertiary referral centre in London. Exclusion criteria for participants were multiple pregnancies, extreme claustrophobia, contraindications for MRI such as pacemakers, and maternal age under 16 or over 55 years. Exclusion criteria for scans were the presence of clear contractions or gross visual artefacts. We performed 68 scans on these pregnant participants on a 0.55T clinical low field scanner with an 80 cm wide bore (MAGNETOM Free.Max, Siemens Healthineers, Erlangen, Germany) after informed consent was obtained (MEERKAT project, REC 19/LO/0852). Participants were scanned in supine position maintaining frequent verbal interaction and life monitoring including heart rate and blood pressure readings. Before scanning each participant with our new

low-field sequence, we performed an initial localiser scan, T2-weighted anatomical imaging, T1 relaxometry and short clinical diffusion sequences. Out of the 68 scans, we excluded 10 scans with clearly visible contractions to eliminate this known source of variation. Although the presence of a contraction does not necessarily render a scan unusable, contractions have been shown to affect T2\* values [29–31], therefore we exclude these scans to leave a dataset with fewer confounding factors. We also excluded one scan since it was a molar pregnancy and one scan due to clear and gross visual artefacts, likely because this placenta was in a fundal position.

This remaining 56 scan cohort comprised 49 distinct participants, with seven participants who were scanned twice over gestation. We obtained detailed clinical information for all participants, including maternal blood pressures and fetal biomarkers from ultrasound monitoring during pregnancy, as well as birth weight centile, type of delivery, and neonatal outcomes. The mean gestational age (GA) at scan time for the final 56 scan cohort was 29.9  $\pm$  5.84 [18.4,41.3] weeks, maternal BMI 28.1  $\pm$  4.84 [18.6, 37.6] kg/m2 and mean maternal age 34.3  $\pm$ 5.19, [24.1, 44.5] years. After collecting the data and clinical information, we grouped all participants into cohorts. We decided to retain all participants, including those with specific pathologies, to maximise the amount of data available for analysis. This results in a heterogeneous cohort with a variety of complications but without large numbers in any single group. Consequently, we cannot make inferences about how well T2\* or ADC discriminate between groups; instead, we present all the data with the aim of demonstrating feasibility. Specifically, we used these clinical details to prospectively categorise the participants into four cohorts. Participants were categorised through holistic investigation of clinical details throughout the entire pregnancy, from recruitment up to and including birth, see Table S1. These cohorts are:

- Syndromes and pregnancy complications: participants with a condition diagnosed clinically either antenatally or postnatally. This cohort comprises 8 participants who underwent 1 scan each.
  Table S1 outlines the specific diagnosis for each patient.
- Brain pathology: participants where a fetal neurological pathology was diagnosed but no additional complications. This cohort comprises 9 participants who underwent 1 scan each. Table S1 outlines the specific diagnosis for each patient.
- 3. T1 diabetes: participants with type 1 diabetes but no additional complications. This cohort comprises 1 participant who underwent 2 scans.
- 4. Healthy controls: all remaining participants. This cohort comprises 31 participants who underwent 37 scans.

Before scanning each participant with our new low-field sequence, we performed an initial localiser scan, T2-weighted anatomical imaging (between 12 and 30 min), T1 relaxometry (3 min) and short clinical diffusion sequences (3 min).

We implemented a combined diffusion-relaxation multi-echo T2\*diffusion scan, using an adapted version of the ZEBRA sequence [32] as previously demonstrated at 3T [24]. We only used automatic shimming, which doesn't require the user to manually highlight an anatomical region for shim optimisation; this manual process is necessary to obtain the best images at 3T [33]. We scanned with two diffusion-weighting schemes, which we denote protocol 1 and protocol 2. Protocol 1 is a subset of protocol 2, with protocol 2 expanded to include more low b-values to better characterise the perfusion component of the signal. For protocol 1, the b-values are 0, 50, 100, 150, 300, 500, 750, 1000 s/mm<sup>2</sup>. For protocol 2, the b-values are 0, 20, 30, 50, 70, 100, 120, 150, 300, 500, 750, 1000 s/mm<sup>2</sup>. For both protocols, each b-value was acquired with three echo times (TEs), 117, 161, 205 ms - these are longer than typical TEs in standard T2\* multi-echo gradient echo scans due to the diffusion gradients - and three orthogonal gradient directions, aligned with the scanner's x, y, and z axes, were acquired for each non-zero b-value-TE pair. Compared to our previous 3T protocols [34],

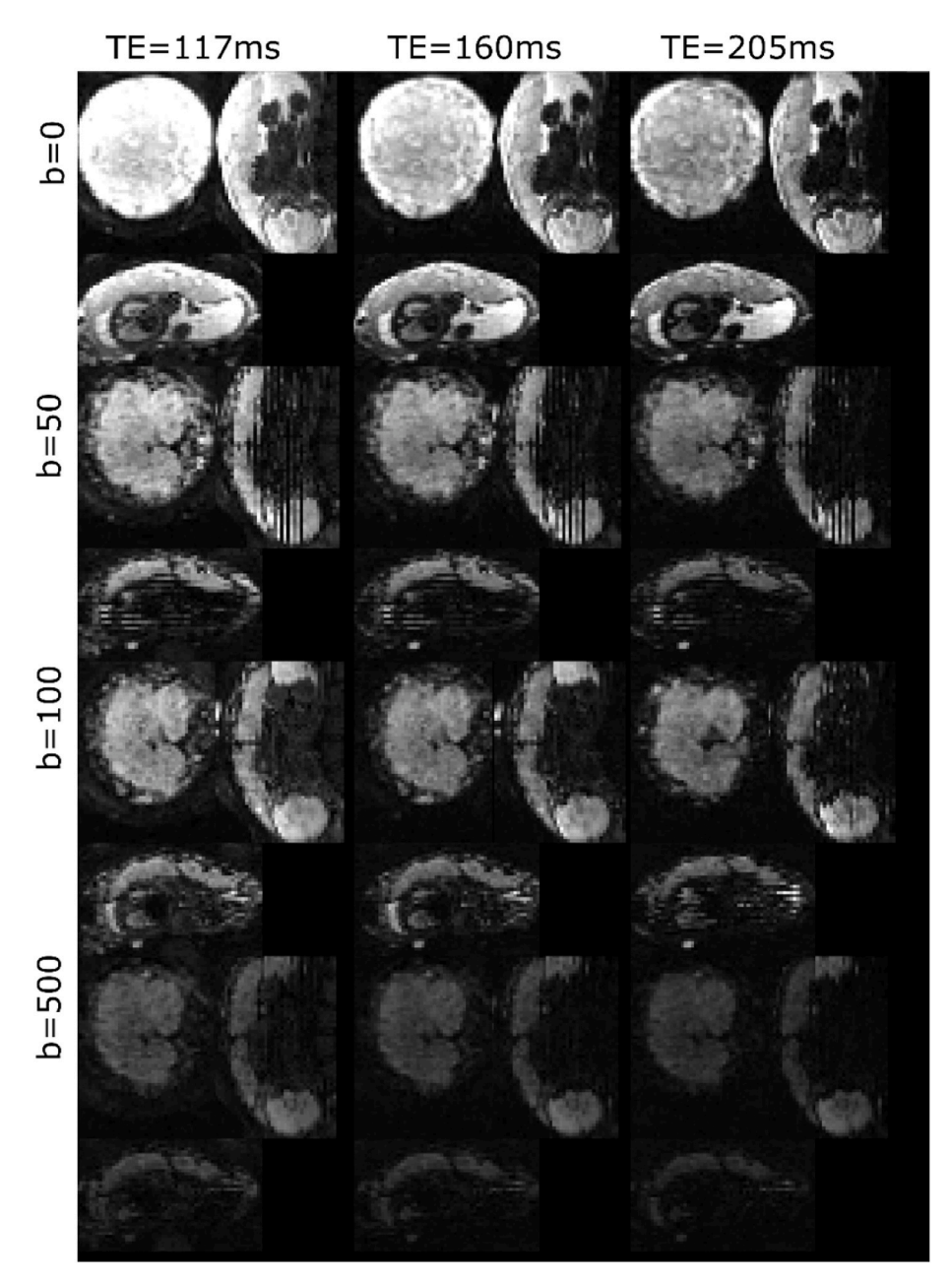


Fig. 1. Exemplary direction-averaged data for three TEs and four b-values after denoising for a single control participant with GA = 27.14 weeks. See Fig. 2 for derived maps for this participant. The dark lines visible in the axial and sagittal planes are due to inter-slice motion.

the highest b-value is lower and the TEs are longer. These adaptations were made to account for the lower SNR and the reduced gradient performance available. The number of b-values and TEs was intentionally kept low to maintain a clinically feasible scan time and ensure the examination is widely available and accessible. Furthermore, the lowest b-value employed on the Free.Max was 20 s/mm<sup>2</sup>, 4 times higher than previously utilised at 3T [24], potentially reducing sensitivity to very high diffusivities associated with perfusion. No B0 map and calibration scans were acquired and no image-based shimming was performed, reducing both the scan time and need for expert knowledge. Scans were acquired in coronal orientation with respect to the mother with a 6-channel surface coil and in-built 9-channel table coil. Other acquisition parameters were: FOV =  $400 \times 400 \times 1600$  mm, 4x4x4mm resolution, Grappa 2, TR = 11.1 s, partial Fourier 7/8, receiver bandwidth = 1162 Hz/Px. Protocol 1 has 66 total volumes and acquisition time 7 min 20 s. Protocol 2 has 102 total volumes and the acquisition time is 11 min. We performed 28 scans with protocol 2. Since protocol 1 is a subset of protocol 2, all 56 scans effectively included protocol 1. Consequently, the protocol 1 portion of the scans could be processed downstream in the same way for all 56 scans.

The data was denoised using the mrtrix [35] implementation of Marchenko-Pastur Principal Component Analysis (MP-PCA) [36] and direction-averaged for each b-TE combination. We analysed the direction-averaged data using a modified version of the dmipy toolbox [37] with a joint T2\*-D model given by

 $S(T2^*, ADC) = S0 \exp(-TE/T2^*) \exp(-b ADC)$ 

where TE and b are the acquired echo times and b-values respectively, T2\* and ADC the obtained T2\* and diffusivity values, and S0 is the signal at the b=0 volume with lowest TE. For the protocol 1 data we fit the model using the full dataset, i.e. all b-TE combinations. For the protocol 2 data, we fit the model to the full dataset, and also to the subset of the protocol corresponding to the protocol 1 b-TE combinations. We therefore obtained 56 protocol 1 T2\* and ADC maps (i.e. all scans), and

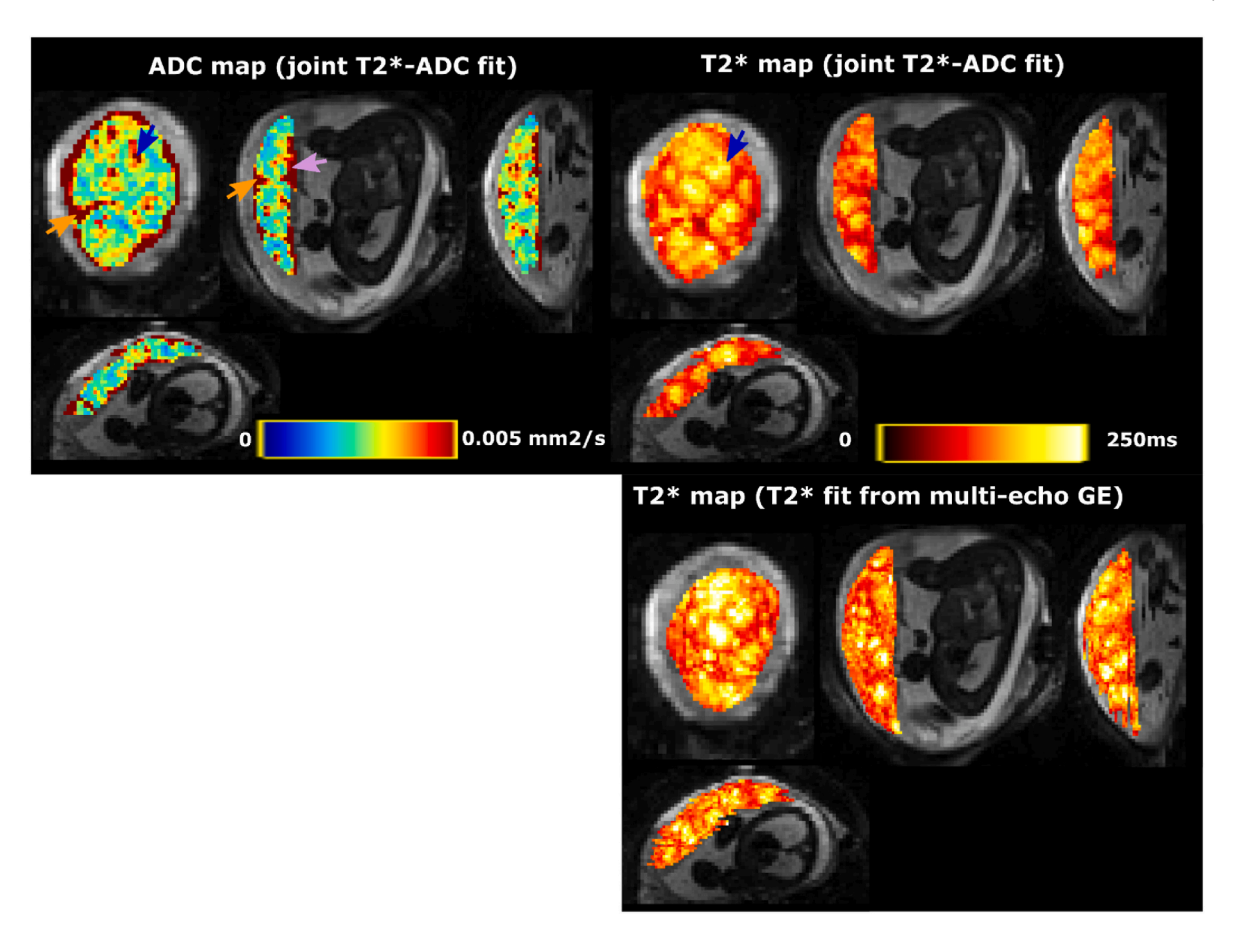


Fig. 2. Detailed view into one example dataset (control, GA = 27.14 weeks - same participant as Fig. 1). Top row: the ADC and  $T2^*$  map from the joint fit. Bottom row: the  $T2^*$  map from the additional multi-echo gradient echo scan. The blue arrow shows the increased ADC and  $T2^*$  in the lobule centres, the pink arrow the increase on the chorionic plate and the orange arrows the increase in ADC and reduction in  $T2^*$  in the septa between the lobules. (For interpretation of the references to color in this figure legend, the reader is referred to the Web version of this article.)

28 protocol 2 T2\* and ADC maps.

We also acquired a separate standard multi-echo gradient echo T2\* scan in all participants, as previously reported [38]. The resolution was  $3x3x3\,$  mm, FOV  $=400\,\times\,400\,\times\,[30\text{-}55]\,$  mm² (slices were added or removed as necessary to maximise placental coverage), TR  $=9670\,$  ms and the TEs were 80 ms, 222 ms and 365 ms. The total acquisition time for one individual volume at all three echo times was 33 s. Of the 56 scans where we acquired combined T2\*-diffusion data, 12 of the corresponding standard multi-echo gradient echo scans contained a clear contraction or visual artifact. As for the T2\*-diffusion scans, we therefore exclude these scans to reduce confounds, leaving 44 matched standard scans. Note that the prevalence of contractions was comparable between combined diffusion-relaxation and standard multi-echo gradient echo field scans. We calculated T2\* maps from these scans with a mono-exponential fit.

We performed a scan-rescan experiment using protocol 2 with an additional participant with  ${\rm GA}=21+5$  weeks. This participant does not form part of the main cohort and is not included in any other graphs or analyses. The participant was scanned once, removed from the scanner, and then scanned again.  ${\rm T2}^*$  and ADC maps were generated using the same pipeline as described earlier.

We also include a matched scan for one participant who was also scanned at 3T in a parallel study. The 3T diffusion-relaxation scanning protocol is given in Ref. [24].

A volumetric ROI containing the whole placenta across all slices where it was visible was defined, ensuring full coverage of the whole organ, was manually defined by a single reader with 10 years of fetal and placental MRI experience (Hutter). We hence calculated the mean

placental T2\* and ADC from the joint T2\*-ADC fit to the combined scan, and the mean placental T2\* for the separate scans. We then fit a linear model to the mean combined scan values against gestational age using numpy's polyfit function.

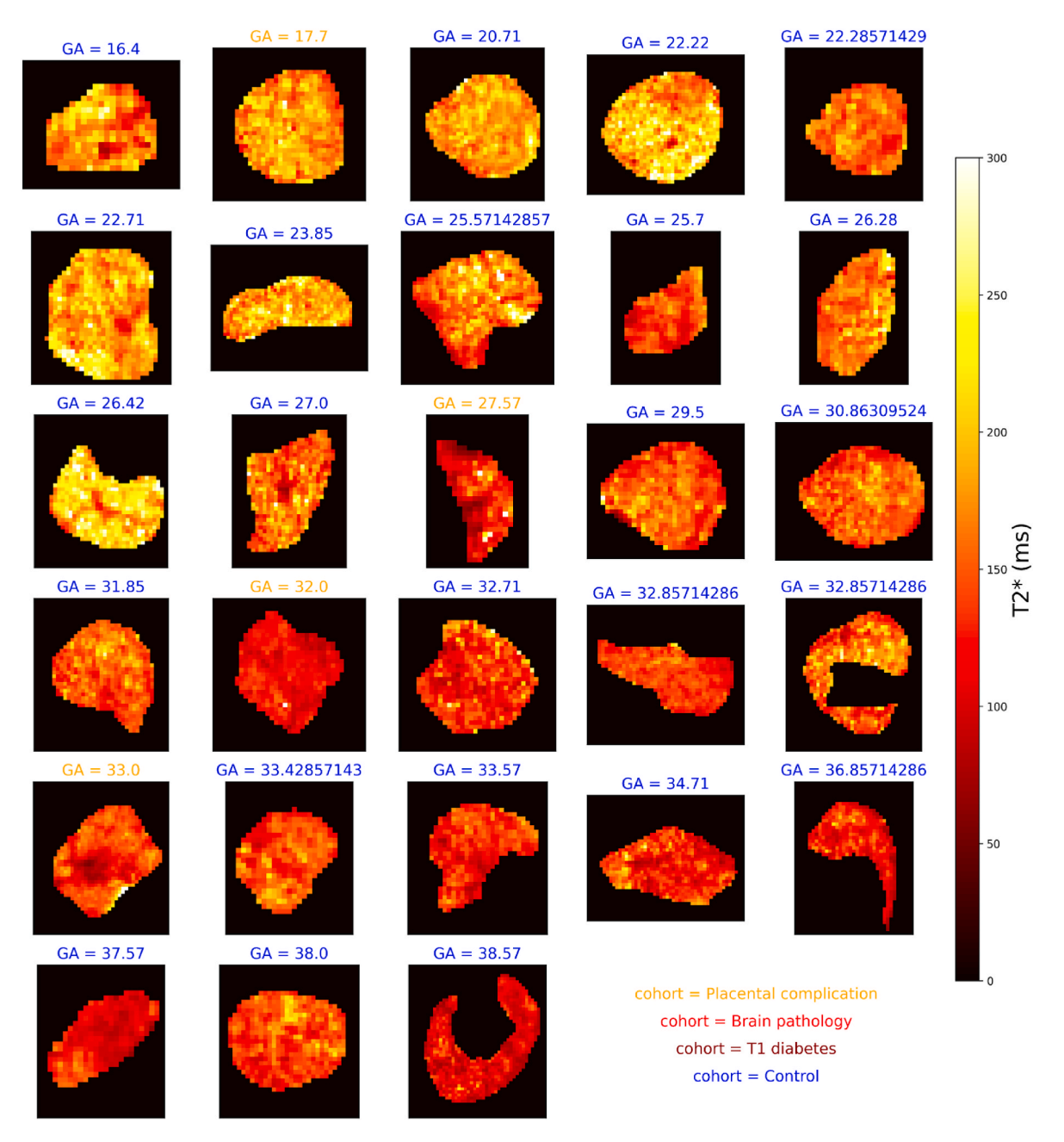
# 3. Results

Fig. 1 shows exemplary direction averaged data for a single scan after denoising. There is clear attenuation with increasing TE - with higher TEs revealing the lobular structure of the placenta. There is also clear signal attenuation with higher b-value, with the signal in the uterine wall attenuating quicker than the signal in the placenta.

Fig. 2 shows example T2\* and diffusivity maps from the T2\*-ADC fit to protocol 1 data for the same participant as Fig. 1. The maps clearly reveal placental features; there are lobular structures revealed in the T2\* map as expected [10], and higher diffusivity at the boundaries of the placenta.

Figs. S2 and S3 show T2\* and diffusivity maps for the T2\*-ADC fits to the protocol 1 data, ordered by gestational age. Figs. 3 and 4 show the same maps for fits to the acquired protocol 2 data. There is a noticeable decrease in T2\* values over gestation, whereas for ADC no clear pattern emerges.

Fig. 5 shows the mean values of  $T2^*$  and ADC in the placenta plotted against gestational age. There is a clear negative trend over gestation for  $T2^*$  for both protocols, but no clear trend over gestation for the ADC. Fig. S5 shows the differences in  $T2^*$  and ADC when estimated from protocol 1 against protocol 2. The ADC estimated with protocol 2 is higher than with protocol 1, likely due to the additional low b-values.



**Fig. 3.** T2\* maps across gestation from joint T2\*-diffusivity model fit to the protocol 2 combined T2\*-diffusion data. Subplot titles give the gestational age in weeks and text color denotes the cohort. Maps show a single mid-placental slice. (For interpretation of the references to color in this figure legend, the reader is referred to the Web version of this article.)

On the other hand, the T2\* estimated with protocol 2 is lower than with protocol 1.

Fig. 6 presents the maps and histograms of the T2\* and ADC from the scan-rescan experiment. The close agreement between the maps and histograms from the two scans serves as demonstration that the scanning and analysis pipeline is stable and reproducible.

Fig. S6 shows mean T2\* values against gestational age for the non-diffusion weighted standard multi-echo gradient echo scans and compares the mean T2\* values between the combined T2\*-diffusion and non-diffusion weighted scans. The left panel of Fig. S6 reveals the same downward trend in T2\* as observed in combined scans, with a slightly lower Pearson coefficient than the combined scan (-0.71 for the standard scan compared to -0.76 and -0.75 for the protocol 1 and protocol 2 combined scans respectively). The middle and right panels of Fig. S6 show that the standard scan routinely estimates higher T2\* than the

combined scans.

Fig. S7 displays the calculated 0.55T and 3T maps for the participant who was also scanned at 3T in a parallel study. Although these images are not co-registered, and the T2\* values differ as expected due to the variation in relaxation times across field strengths, there are reasonably consistent patterns in the ADC and T2\* maps. For instance, regions with high ADC and high T2\* are visible along the boundaries of the placenta in the second row of Fig. S7.

# 4. Discussion

Our study demonstrates quantitative placental MRI at 0.55 T, which offers several advantages over high-field scanning for the purpose of pregnancy monitoring. In addition to the potential for reduced cost and thus increased accessibility, low-field MRI can address specific issues

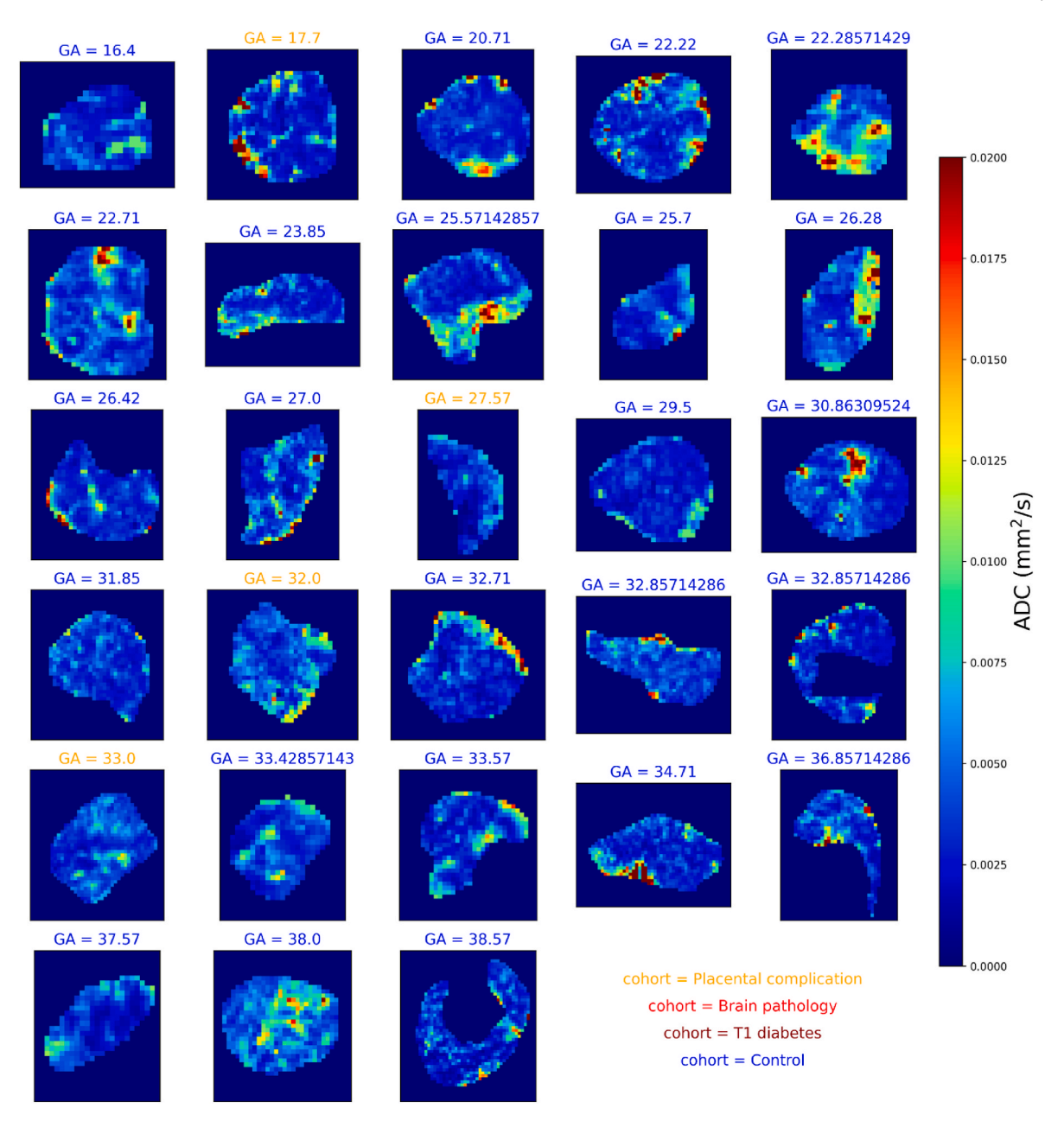


Fig. 4. Diffusivity maps across gestation from joint T2\*-diffusivity model fit to the protocol 2 combined T2\*-diffusion data. Subplot titles give the gestational age in weeks and text color denotes the cohort. Maps show the mid-placental slice as Fig. 3. (For interpretation of the references to color in this figure legend, the reader is referred to the Web version of this article.)

related to pregnancy, such as a larger bore size allowing access to this modality for the growing number of overweight and women with obesity, and reduced distortion artefacts and B1 inhomogeneity, addressing some image quality challenges in abdominal/fetal MRI and foregoing the need for specialist shimming tools and expertise. However, it is important to note that these advantages come with trade-offs. Lowfield MRI has several disadvantages compared to high-field, including significantly lower SNR, which necessitates the use of larger voxels to maintain sufficient signal, which in turn reduces image resolution. Deriving quantitative metrics from low-field MRI could potentially enable early and specific diagnosis of pregnancy complications, including pre-eclampsia and FGR. Although we emphasise that the small number scans with complications prevent us from making definitive statements about the utility of low field combined T2\*-diffusion MRI from this study alone, we note that this approach is promising and warrants further exploration, as low field MRI can be deployed in a

much broader range of settings than high-field MRI alone. This could significantly improve pregnancy monitoring and management, especially in low-resource settings.

On first inspection, our 0.55T scans contain similar information to previous work at 1.5T and 3T. Namely, the measured low-field T2\* and diffusivity maps (Figs. 2–4, Figs. S2 and S3) have comparable patterns to those previously observed at higher field strengths and for separate T2\* scans [39]; for example, the T2\* clearly decreases over gestational age and some ADC maps show bright patches at the placental boundaries. We emphasise that our findings regarding how these parameters change over gestation are not novel in themselves, but we show these trends for the first time in a combined T2\*-diffusion experiment at low field. Maps from a single participant who was scanned at 0.55T and 3T also show reasonable agreement, with high ADC and T2\* patches appearing in similar areas (Fig. S7). This is despite different scanning parameters such as the voxel size (4 mm³ isotropic here compared to  $\sim$ 2 mm³ at 3T, e.g.

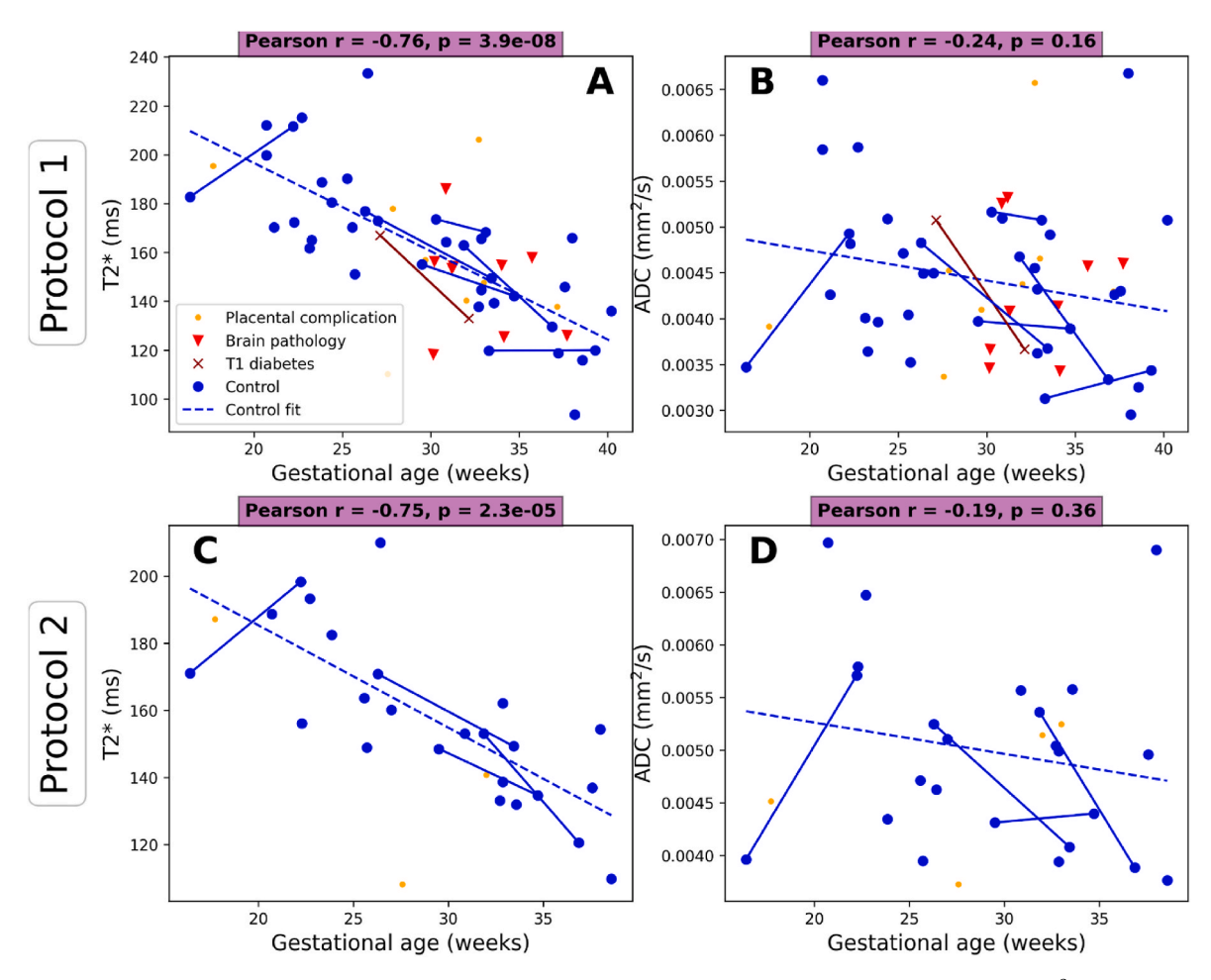


Fig. 5. Mean  $T2^*$  and ADC values over gestational age across the cohorts for protocol 1 (b = 0, 50, 100, 150, 300, 500, 750, 1000 s/mm<sup>2</sup>) and protocol 2 (b = 0, 20, 30, 50, 70, 100, 120 150, 300, 500, 750, 1000 s/mm<sup>2</sup>). Solid lines indicate the same participant scanned twice. Dashed line shows linear fit to the control data. Parameters of the fitted lines are given in Table S4. Note that a single outlier datapoint is cut off from panel A.

Ref. [24]). Many T2\* maps (Figs. 2 and 3, Fig. S2) reveal the lobular structure of the placenta, potentially revealing the oxygenation level of maternal blood, as previously observed in standard T2\* [7,40,41] and combined T2\*-diffusion [24,25] experiments. There is also a higher diffusivity at the boundaries of the placenta in ADC maps potentially reflecting areas with high volumes of maternal blood perfusing into the placenta (Fig. 4 and Fig. S3). This was previously shown in diffusion [34] and combined T2\*-diffusion [24,25] scans. These observations highlight that combined T2\*-diffusion MRI at 0.55T is viable and promising.

As expected, the T2\* values calculated from our 0.55T scans are higher than those previously reported at higher field strengths. An extensive quantitative comparison of T2\* values across field strengths for standard gradient echo sequences was undertaken by Hall et al. [39]. They reported predicted values for T2\* at 0.55 T as 245 ms, 200 ms, and 152 ms at 20, 30, and 40 weeks respectively. For comparison, their predicted T2\* values at 3T were 98 ms, 60 ms, and 25 ms at 20, 30, and 40 weeks respectively, and their predicted T2\* values at 1.5T were 160 ms, 110 ms and 70 ms 20, 30, and 40 weeks respectively. Visual inspection of Fig. S6A confirms that our standard multi-echo gradient echo T2\* values are in line with these. However, since the standard T2\* scans in this paper are a subset of the Hall et al. dataset, this serves as a sanity check rather than an external validation.

The expected  $T2^*$  values from a linear fit to the mean placental  $T2^*$  values from combined  $T2^*$ -diffusion scans are given in Table S8, and are lower than those from Hall et al. When directly comparing combined and separate scans from the same participant, we again found that

measuring T2\* with a standard, separate T2\* scan routinely estimates higher T2\* than the combined scan (Fig. S6B–C). We also observed that the combined T2\*-diffusion protocol with more b-values (protocol 2) results in higher ADC and lower T2\* values (Fig. S5). This may reflect the fact that the current model does not account for IVIM effects. In future, we will apply combined diffusion-relaxation models that incorporate these, such as those demonstrated in Ref. [25]. Additionally, combined T2\*-diffusion scans may inherently yield different values than separate T2\* scans, due to a portion of the T2\* decay being fit by the diffusion component of the model and vice-versa. The extent to which the separate and/or combined scans reflect the true, underlying, T2\* value is an open question that warrants further investigation, by first undertaking combined and standard scans with matched TEs.

An interesting observation across both this study and Hall et al. is that despite having fewer echo times, we observe a potentially wider absolute range in T2\* values across gestational age at 0.55T likely due to these longer relaxation times. This may allow for better quantification of more subtle and individual differences in oxygenation in pregnancy complications where T2\* is reduced [12], by enabling wider separation of controls and cases. A further disadvantage of larger voxels is their impact on regional T2\* analyses. While the mean T2\* across the whole placenta may not differ significantly with larger voxels, analyses involving histograms of T2\* values or spatial T2\* maps will likely be affected by the voxel size.

We removed several scans from the analysis due to clearly visible contractions, since it is known that contractions affect the T2\* value [29–31]. In future, we will explore methods to limit the influence of

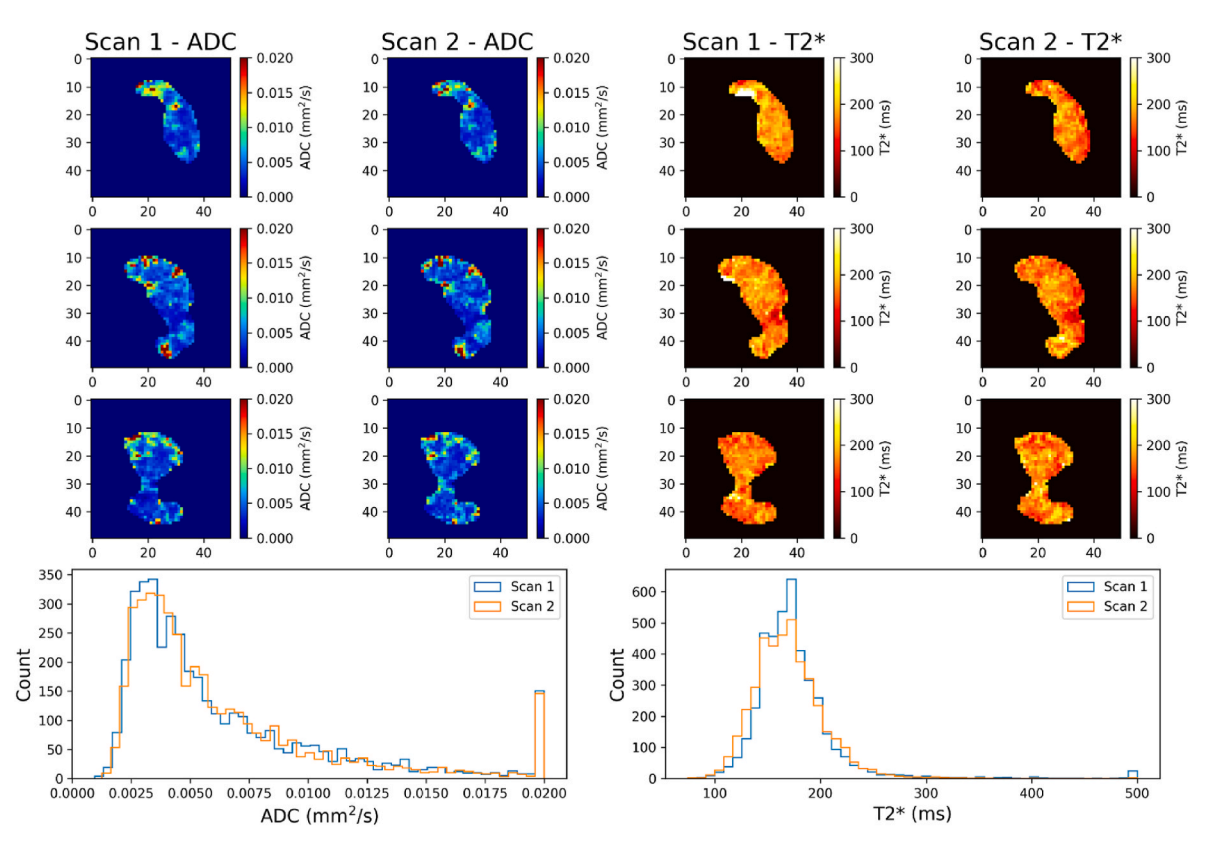


Fig. 6. Scan-rescan results from a single control participant with GA = 21 + 5 weeks. Top rows: ADC and T2\* maps Bottom row: ADC and T2\* histograms.

contractions on the scans and ensure that interpretable data can still be obtained despite their occurrence. It is possible that contractions are not entirely detrimental; their effect on T2\* may provide valuable information about placental health and function.

## 5. Limitations and future work

The presented results hint that low-field ADC and T2\* maps display wider across-scan variance than those obtained at high field. This could be because our preprocessing pipeline is not as extensive as those used at higher field strengths. Whilst we did denoise the data, we did not perform motion correction, as we have not yet developed low-field-specific algorithms that account for the larger voxel size and lower resolution. In future, we will continue building our pre-processing pipelines for low-field placental MRI by developing and integrating low-field specific methods for motion correction and artifact correction.

This study has reduced b-value coverage, particularly at very low b-values, to previous studies at higher field strength. For example, the minimum b-value in Ref. [34] was  $5\,\mathrm{s/mm^2}$  compared to  $20\,\mathrm{or}\,50\,\mathrm{s/mm^2}$  here. This may lead to diffusivity maps with lower ranges than in comparable studies at 1.5 T and 3 T. An obvious path for further investigation is to collect repeat combined T2\*-diffusion (and separate T2\*) measurements for the same participants on the same day at 0.55 T, 1.5 T, and 3 T.

We assumed that T2\* and diffusion decays are both monoexponential. This is suboptimal, particularly as it has been previously shown that multi-compartment models are required to adequately explain the diffusion MRI signal in the placenta [34]. In future we will explore such models, as previously demonstrated in T2-diffusion [23, 26] and T2\*-diffusion [25] experiments. Although in principle we could also explore multi-exponential decay models of the T2\* signal, in practice this would likely require more TEs than the current three. As well as multi-compartment modelling, we will also explore data-driven unsupervised machine learning approaches that don't require fixing the number of model compartments [42]. We will also assess the goodness of fit and appropriateness of the models using model selection procedures to determine which model best explains the data. This can also evaluate the relative strengths of T2\* and diffusion metrics in diagnosing pregnancy complications and determine whether longer combined scans are necessary or if a single T2\* or diffusion scan would suffice.

In this study, we scanned coronally to the maternal habitus and displayed parameter maps of the largest slice through the placental parenchyma (in Figs. 2–4). In future, specific visualisation and analysis of the whole placenta including spiral arteries and chorionic plate would be simplified by transforming the placenta into a common, biological space as previously proposed [43,44].

We demonstrated that the estimated T2\* values differ between individual gradient echo scans and combined T2\*-diffusion scans (Fig. S6) as well as between protocol 1 and protocol 2 combined T2\*-diffusion scans (Fig. S5). Additionally, the ADC values vary between protocol 1 and protocol 2 (Fig. S5). This variation is expected to some extent since different b-values and different TEs probe different diffusion and relaxation regimes. A major step towards addressing these challenges in a clinical setting will be to fix the b-values and TEs to optimal settings for assessing pregnancy complications, but this first requires determining what these optimal settings are.

The data we present in this study is insufficient to demonstrate that T2\* or ADC from combined T2\*-diffusion scans at low field can reliably identify pregnancy complications. The limited number of non-control scans necessitated broad cohort definitions, potentially masking subtle differences. Despite this, we remain optimistic that further studies with larger and more specifically defined cohorts will reveal biomarkers for specific pregnancy complications. Our optimism is backed up by the fact that T2\* calculated from a standard multi-echo gradient echo scan does not show clear separation between our cohorts, despite strong evidence in the literature showing that placental T2\* is a biomarker for pregnancy complications. An obvious and compelling avenue for further research involves conducting a multi-centre study with a larger participant pool,

including a wider range of fine-grained pregnancy-related complications, rather than the broad categorisation of complications we use here. This study would have increased statistical power and could identify more nuanced relationships between placental MRI metrics and specific pregnancy complications.

#### 6. Conclusion

We demonstrate placental quantitative MRI at 0.55T. Our results show many common features with studies conducted at higher field strengths; parameter maps have similar patterns and there are similar trends in T2\* and ADC across gestational age. Our findings can initiate broader research into quantitative placental MRI at low-field, with the long-term goal of complementing ultrasound in pregnancy monitoring.

#### CRediT authorship contribution statement

Paddy J. Slator: Writing – review & editing, Writing – original draft, Visualization, Software, Methodology, Investigation, Formal analysis, Conceptualization. Jordina Aviles Verdera: Methodology, Data curation, Conceptualization. Raphael Tomi-Tricot: Data curation, Conceptualization. Joseph V. Hajnal: Funding acquisition, Conceptualization. Daniel C. Alexander: Writing – review & editing, Funding acquisition. Jana Hutter: Writing – review & editing, Writing – original draft, Visualization, Software, Methodology, Formal analysis, Data curation, Conceptualization.

# Declaration of generative AI and AI-assisted technologies in the writing process

During the preparation of this work the authors used ChatGPT to suggest alternative phrasings and check for spelling and grammatical errors. After using this tool/service, the authors reviewed and edited the content as needed and take full responsibility for the content of the publication.

# Declaration of competing interest

Raphael Tomi-Tricot is an employee of Siemens Healthineers.

## Acknowledgements

We thank all pregnant participants, midwives, obstetricians, and radiographers who played a key role in obtaining the datasets. Grant support: NIH (1U01HD087202-01); Wellcome Trust (201374/Z/16/Z); EPSRC (EP/V034537/1, EP/M020533/1); UKRI (MR/T018119/1 JH); MRC (MR/V002465/1); NIHR Biomedical Research Centre at UCLH NHS Foundation Trust and UCL; core funding from the Wellcome/EPSRC Centre for Medical Engineering at KCL (WT 203148/Z/16/Z); the NIHR Biomedical Research Centre based at Guy's and St Thomas' NHS Foundation Trust and KCL. The views expressed are those of the authors and not necessarily those of the NHS, the NIHR or the Department of Health.

# Appendix A. Supplementary data

Supplementary data to this article can be found online at https://doi.org/10.1016/j.placenta.2025.10.014.

## References

- [1] G.J. Burton, E. Jauniaux, What is the placenta? Am. J. Obstet. Gynecol. 213 (2015) S6.e1–S6.e4, https://doi.org/10.1016/j.ajog.2015.07.050.
- [2] G.J. Burton, A.L. Fowden, The placenta: a multifaceted, transient organ, Phil. Trans. Biol. Sci. 370 (2015) 20140066, https://doi.org/10.1098/rstb.2014.0066, 20140066.

[3] I. Brosens, R. Pijnenborg, L. Vercruysse, R. Romero, The "Great Obstetrical Syndromes" are associated with disorders of deep placentation, Am. J. Obstet. Gynecol. 204 (2011) 193–201, https://doi.org/10.1016/J.AJOG.2010.08.009.

- [4] M.Y. Turco, A. Moffett, Development of the human placenta, Development 146 (2019) dev163428, https://doi.org/10.1242/dev.163428.
- [5] D.L. Rolnik, D. Wright, L.C. Poon, N. O'Gorman, A. Syngelaki, Matallana C. de Paco, et al., Aspirin versus placebo in pregnancies at high risk for Preterm Preeclampsia, N. Engl. J. Med. 377 (2017) 613–622, https://doi.org/10.1056/ NEJMoa1704559
- [6] M. Sinding, D.A. Peters, J.B. Frøkjaer, O.B. Christiansen, A. Petersen, N. Uldbjerg, et al., Placental magnetic resonance imaging T2\* measurements in normal pregnancies and in those complicated by fetal growth restriction, Ultrasound Obstet. Gynecol. 47 (2016) 748–754, https://doi.org/10.1002/uog.14917.
- [7] A.E.P. Ho, J. Hutter, L.H. Jackson, P.T. Seed, L. McCabe, M. Al-Adnani, et al., T2\* placental magnetic resonance imaging in Preterm Preeclampsia: an observational cohort Study, Hypertension 75 (2020) 1523–1531, https://doi.org/10.1161/ HYPERTENSIONAHA.120.14701.
- [8] I. Huen, D.M. Morris, C. Wright, G.J.M. Parker, C.P. Sibley, E.D. Johnstone, et al., R1 and R2\* changes in the human placenta in response to maternal oxygen challenge, Magn. Reson. Med. 70 (2013) 1427–1433, https://doi.org/10.1002/ mrm.24581.
- [9] R. Avni, O. Golani, A. Akselrod-Ballin, Y. Cohen, I. Biton, J.R. Garbow, et al., MR imaging-derived oxygen-hemoglobin dissociation curves and fetal-placental oxygen-hemoglobin affinities, Radiology 280 (2016) 68–77, https://doi.org/ 10.1148/radiol.2015150721.
- [10] M.C. Schabel, V.H.J. Roberts, J.O. Lo, S. Platt, K.A. Grant, A.E. Frias, et al., Functional imaging of the nonhuman primate Placenta with endogenous blood oxygen level-dependent contrast, Magn. Reson. Med. 76 (2016) 1551–1562, https://doi.org/10.1002/mrm.26052.
- [11] M.C. Schabel, V.H.J. Roberts, K.J. Gibbins, M. Rincon, J.E. Gaffney, A.D. Streblow, et al., Quantitative longitudinal T2\* mapping for assessing placental function and association with adverse pregnancy outcomes across gestation. Stevenson GN, PLoS One 17 (2022) e0270360, https://doi.org/10.1371/journal.pone.0270360.
- [12] A. Sørensen, J. Hutter, M. Seed, P.E. Grant, P. Gowland, T2\*-weighted placental MRI: basic research tool or emerging clinical test for placental dysfunction? Ultrasound Obstet. Gynecol. 55 (2020) 293–302, https://doi.org/10.1002/ uog. 20855.
- [13] J.O. Lo, V.H.J. Roberts, M.C. Schabel, X. Wang, T.K. Morgan, Z. Liu, et al., Novel detection of placental insufficiency by magnetic resonance imaging in the Nonhuman primate, Reprod. Sci. 25 (2017), https://doi.org/10.1177/1933719117699704, 193371911769970-193371911769970.
- [14] H.M. Bonel, B. Stolz, L. Diedrichsen, K. Frei, B. Saar, B. Tutschek, et al., Diffusion-weighted MR imaging of the placenta in fetuses with placental insufficiency, Radiology 257 (2010) 810–819, https://doi.org/10.1148/radiol.10092283.
- [15] S.B. Gorkem, A. Coskun, M. Eslik, M.S. Kutuk, A. Ozturk, Diffusion-weighted imaging of placenta in intrauterine growth restriction with worsening Doppler US findings, Diagn. Interv. Radiol. 25 (2019) 280–284, https://doi.org/10.5152/ dir.2019.18358
- [16] F. Song, W. Wu, Z. Qian, G. Zhang, Y. Cheng, Assessment of the placenta in intrauterine growth restriction by diffusion-weighted imaging and Proton magnetic resonance spectroscopy, Reprod. Sci. 24 (2017) 575–581, https://doi.org/ 10.1177/1933719116667219.
- [17] R.J. Moore, B.K. Strachan, D.J. Tyler, K.R. Duncan, P.N. Baker, B.S. Worthington, et al., In utero perfusing fraction maps in normal and growth restricted pregnancy measured using IVIM Echo-Planar MRI, Placenta 21 (2000) 726–732, https://doi.org/10.1053/plac.2000.0567.
- [18] I. Derwig, D.J. Lythgoe, G.J. Barker, L. Poon, P. Gowland, R. Yeung, et al., Association of placental perfusion, as assessed by magnetic resonance imaging and uterine artery Doppler ultrasound, and its relationship to pregnancy outcome, Placenta 34 (2013) 885–891, https://doi.org/10.1016/j.placenta.2013.07.006.
- [19] M. Malmberg, E. Kragsterman, M. Sinding, D.N. Hansen, D.A. Peters, J.B. Frøkjær, et al., Perfusion fraction derived from IVIM analysis of diffusion-weighted MRI in the assessment of placental vascular malperfusion antenatally, Placenta 119 (2022) 1–7, https://doi.org/10.1016/j.placenta.2022.01.005.
- [20] H. Li, L. Liang, A. Li, Y. Hu, D. Hu, Z. Li, et al., Monoexponential, biexponential, and stretched exponential diffusion-weighted imaging models: quantitative biomarkers for differentiating renal clear cell carcinoma and minimal fat angiomyolipoma: imaging Models for differentiating ccRCC and MFAML, J. Magn. Reson. Imag. 46 (2017) 240–247, https://doi.org/10.1002/jmri.25524.
- [21] B.A. Kristi, N.H. Ditte, H. Caroline, S. Marianne, P. Astrid, B.F. Jens, et al., Placental diffusion-weighted MRI in normal pregnancies and those complicated by placental dysfunction due to vascular malperfusion, Placenta 91 (2020) 52–58, https://doi.org/10.1016/j.placenta.2020.01.009.
- [22] P.J. Slator, M. Palombo, K.L. Miller, C.F. Westin, F. Laun, D. Kim, et al., Combined diffusion-relaxometry microstructure imaging: current status and future prospects, Magn. Reson. Med. (2021) 1–25, https://doi.org/10.1002/mrm.28963.
- [23] A. Melbourne, R. Aughwane, M. Sokolska, D. Owen, G. Kendall, D. Flouri, et al., Separating fetal and maternal placenta circulations using multiparametric MRI, Magn. Reson. Med. 81 (2018) 350–361, https://doi.org/10.1002/mrm.27406.
- [24] P.J. Slator, J. Hutter, M. Palombo, L.H. Jackson, A. Ho, E. Panagiotaki, et al., Combined diffusion-relaxometry MRI to identify dysfunction in the human placenta, Magn. Reson. Med. (2019) 1–22, https://doi.org/10.1002/mrm.27733
- [25] D. Cromb, P.J. Slator, M. De La Fuente, A.N. Price, M. Rutherford, A. Egloff, et al., Assessing within-subject rates of change of placental MRI diffusion metrics in normal pregnancy, Magn. Reson. Med. 90 (2023) 1137–1150, https://doi.org/ 10.1002/mrm.29665.

- [26] R. Aughwane, N. Mufti, D. Flouri, K. Maksym, R. Spencer, M. Sokolska, et al., Magnetic resonance imaging measurement of placental perfusion and oxygen saturation in early-onset fetal growth restriction, BJOG Int. J. Obstet. Gynaecol. 128 (2021) 337–345, https://doi.org/10.1111/1471-0528.16387.
- [27] M. Hori, A. Hagiwara, M. Goto, A. Wada, S. Aoki, Low-Field magnetic resonance imaging: its history and Renaissance, Investig. Radiol. 56 (2021) 669–679, https://doi.org/10.1097/RLI.000000000000810.
- [28] J. Vosshenrich, H.-C. Breit, M. Bach, E.M. Merkle, Ökonomische Aspekte der Niederfeld-Magnetresonanztomographie: Anschaffung, Installation und Unterhaltskosten von 0,55 T-Geräten, Radiologe 62 (2022) 400–404, https://doi. org/10.1007/s00117-022-00986-9.
- [29] Turk E. Abaci, S.M. Abulnaga, J. Luo, J.N. Stout, H.A. Feldman, A. Turk, et al., Placental MRI: effect of maternal position and uterine contractions on placental BOLD MRI measurements, Placenta 95 (2020) 69–77, https://doi.org/10.1016/j. placenta.2020.04.008.
- [30] J. Hutter, V. Kohli, N. Dellschaft, A. Uus, L. Story, J.K. Steinweg, et al., Dynamics of T2\* and deformation in the placenta and myometrium during pre-labour contractions, Sci. Rep. 12 (2022) 18542, https://doi.org/10.1038/s41598-022-22008-3.
- [31] N.S. Dellschaft, G. Hutchinson, S. Shah, N.W. Jones, C. Bradley, L. Leach, et al., The haemodynamics of the human placenta in utero, in: M. Ikawa (Ed.), PLoS Biol. 18 (2020), https://doi.org/10.1371/journal.pbio.3000676 e3000676-e3000676.
- [32] J. Hutter, P.J. Slator, D. Christiaens, R.P.A.G. Teixeira, T. Roberts, L. Jackson, et al., Integrated and efficient diffusion-relaxometry using ZEBRA, Sci. Rep. 8 (2018), https://doi.org/10.1038/s41598-018-33463-2, 15138-15138.
- [33] A.S. Gaspar, R.G. Nunes, G. Ferrazzi, E.J. Hughes, J. Hutter, S.J. Malik, et al., Optimizing maternal fat suppression with constrained image-based shimming in fetal MR, Magn. Reson. Med. 81 (2019) 477–485, https://doi.org/10.1002/ mrm 27375
- [34] P.J. Slator, J. Hutter, L. McCabe, A.D.S. Gomes, A.N. Price, E. Panagiotaki, et al., Placenta microstructure and microcirculation imaging with diffusion MRI, Magn. Reson. Med. 80 (2018) 756–766, https://doi.org/10.1002/mrm.27036.
- [35] J.-D. Tournier, R. Smith, D. Raffelt, R. Tabbara, T. Dhollander, M. Pietsch, et al., MRtrix3: a fast. flexible and open software framework for medical image

- processing and visualisation, Neuroimage 202 (2019), https://doi.org/10.1016/j.neuroimage.2019.116137, 116137–116137.
- [36] J. Veraart, D.S. Novikov, D. Christiaens, B. Ades-aron, J. Sijbers, E. Fieremans, Denoising of diffusion MRI using random matrix theory, Neuroimage 142 (2016) 394–406, https://doi.org/10.1016/j.neuroimage.2016.08.016.
- [37] R.H.J. Fick, D. Wassermann, R. Deriche, The dmipy toolbox: diffusion MRI multicompartment modeling and microstructure recovery made easy, Front. Neuroinf. 13 (2019) 1–26, https://doi.org/10.3389/fninf.2019.00064.
- [38] J. Aviles, K. Colford, M. Hall, M. Marenzana, A. Uus, S. Giles, et al., A fast anatomical and quantitative MRI fetal exam at low field, in: R. Licandro, A. Melbourne, E. Abaci Turk, C. Macgowan, J. Hutter (Eds.), Perinatal, Preterm and Paediatric Image Analysis, Springer Nature Switzerland, Cham, 2022, pp. 13–24, https://doi.org/10.1007/978-3-031-17117-8 2.
- [39] M. Hall, J.A. Verdera, D. Cromb, S.N. Silva, M. Rutherford, S.J. Counsell, et al., Placental T2\* as a measure of placental function across field strength from 0.55T to 3T, Sci. Rep. 14 (2024) 28594, https://doi.org/10.1038/s41598-024-77406-6.
- [40] J. Hutter, P.J. Slator, L. Jackson, A.D.S. Gomes, A. Ho, L. Story, et al., Multi-modal functional MRI to explore placental function over gestation, Magn. Reson. Med. 81 (2019) 1191–1204, https://doi.org/10.1002/mrm.27447.
- [41] J. Hutter, L. Jackson, A. Ho, C. Avena Zampieri, J.V. Hajnal, M. Al-Adnani, et al., The use of functional placental magnetic resonance imaging for assessment of the placenta after prolonged preterm rupture of the membranes in vivo: a pilot study, Acta Obstet. Gynecol. Scand. 100 (2021) 2244–2252, https://doi.org/10.1111/ aogs.14267.
- [42] P.J. Slator, J. Hutter, R.V. Marinescu, M. Palombo, L.H. Jackson, A. Ho, et al., Data-Driven multi-contrast spectral microstructure imaging with InSpect: integrated SPECTral component estimation and mapping, Med. Image Anal. 71 (2021), https://doi.org/10.1016/j.media.2021.102045, 102045–102045.
- [43] S.M. Abulnaga, E.A. Turk, M. Bessmeltsev, P.E. Grant, J. Solomon, P. Golland, Volumetric parameterization of the placenta to a flattened template, IEEE Trans. Med. Imag. 41 (2022) 925–936, https://doi.org/10.1109/TMI.2021.3128743.
- [44] H. Miao, G. Mistelbauer, A. Karimov, A. Alansary, A. Davidson, D.F.A. Lloyd, et al., Placenta maps: in utero placental health assessment of the human fetus, IEEE Trans. Vis. Comput. Graph. 23 (2017) 1612–1623, https://doi.org/10.1109/ TVCG.2017.2674938.